

# Spherical Near-Field Alignment Sensitivity for Polar and Equatorial Antenna Measurements

Patrick Pelland, Greg Hindman,  
Daniël Janse van Rensburg  
NSI-MI Technologies LLC

ppelland@nsi-mi.com, ghindman@nsi-mi.com, drensburg@nsi-mi.com

**Abstract** — Spherical near-field (SNF) antenna test systems offer unique advantages over other types of measurement configurations and have become increasingly popular as a result. To yield accurate far-field radiation patterns, it is critical that the rotators of the SNF scanner are properly aligned. Many techniques using optical instruments, laser trackers, low cost devices or even electrical measurements have been developed to align these systems. While these alignment procedures have been used in practice with great success, some residual alignment errors always remain. This paper expands on prior work by analyzing the effects of spherical alignment errors for a variety of different measurement grids on a theta-over-phi SNF scanner. Results are presented using a combination of physical alignment perturbations (measured) and errors induced via simulation. A variety of antenna types and directions of radiation within the measurement sphere are considered.

**Index Terms** — spherical, near-field, alignment, measurement, errors.

## I. INTRODUCTION

Spherical near-field (SNF) antenna test systems offer unique advantages over other types of measurement configurations. Unlike planar and cylindrical near-field geometries the spherical geometry is capable of accurately characterizing an antenna's radiation pattern over a full sphere. The lack of near-field data truncation leaves side lobes unaffected as well as the antenna's back lobe structure. Additionally, SNF measurements are ideal for testing low gain antennas when far-field testing is not an option.

To yield high accuracy far-field radiation patterns, it is critical that the rotators of the SNF scanner are well-aligned. For very large systems, this alignment is usually accomplished using optical instruments such as theodolites [2] or more recently, laser trackers. Low cost, high accuracy alignment techniques have also been developed for smaller SNF scanners [1] and have been used in practice with great success. When mechanical alignment tools are not available or a periodic scanner re-alignment is required, an electrical technique has also been developed [3]. This alignment can be performed with the actual AUT and probe mounted on their respective positioners.

To quantify the effects of various misalignments in SNF antenna measurements, studies were conducted by intentionally introducing errors to a well-aligned scanner [4]. These perturbations included, but were not limited to

- 1) Non-orthogonality of the  $\theta$  and  $\phi$  axes.
- 2) Non-intersection of the  $\theta$  and  $\phi$  axes.
- 3)  $\theta$ -zero position error.

This work also showed a variation in alignment sensitivity, dependent on the particular spherical acquisition grid selected. We expand on the research described in [3, 4] by analyzing the effects of spherical alignment errors for a variety of different measurement grids, using a theta-over-phi ( $\theta/\phi$ ) swing arm type SNF scanner. Additionally, measurements will be performed with an AUT pointed at the pole of the measurement sphere ( $\theta = 0^\circ$ , polar-mode) and the equator of the sphere ( $\theta = 90^\circ$ , equatorial-mode). These different radiation conditions explore to notion of a varied alignment sensitivity, based on the direction of AUT radiation observed before.

## II. CRITICAL ALIGNMENT PARAMETERS IN SNF MEASUREMENTS

When aligned perfectly, an SNF test system should rotate the AUT and/or probe in such a way that data is acquired over a true spherical surface. In practice, alignment errors will cause data to be acquired over an imperfect spherical surface. Some critical alignment parameters include; axis non-intersection, axis orthogonality and the definition of the  $\theta = 0^\circ$  position. For a complete description of alignment errors for SNF systems see [4, 5, 7 & 10].

## III. SNF MEASUREMENT GEOMETRIES AND IMPLEMENTATION CONFIGURATIONS

A variety of SNF implementations is available to acquire data over all or part of a spherical surface. However, regardless of the specific implementation, the notion of being able to acquire each and every data point in two distinct ways is essential to understand first.

### A. SNF Measurement Geometries

In order to generate a single unique spherical grid of data, the theta ( $\theta$ ) or phi ( $\phi$ ) axis needs to be capable of rotating  $360^\circ$  while the other only needs to rotate  $180^\circ$  to close the surface of the sphere. One option that will achieve that is:

$$-180^\circ \leq \theta \leq +180^\circ, 0^\circ \leq \phi \leq 180^\circ$$

A second alternative option that will achieve that is:

$$0^\circ \leq \theta \leq +180^\circ, 0^\circ \leq \phi \leq 360^\circ$$

Amplitude and phase information is collected at points on either of these spherical grids and transformed to the far-field. These two grids are referred to as the 180- $\phi$  and 360- $\phi$ , respectively.

Both of these grids will result in valid far-field radiation patterns but are affected by room scattering and alignment errors in different ways [5, 6, 7, 8]. A third and important alternative is when both  $\theta$  and  $\phi$  axes are allowed to rotate a full 360°, resulting in a redundant sphere of data:

$$-180^\circ \leq \theta \leq +180^\circ, 0^\circ \leq \phi \leq 360^\circ$$

This measurement geometry has been shown to reduce the effects of room scattering but its sensitivity to alignment errors is not well documented. Figure 1. illustrates the differences between these three grids for a sample amplitude pattern of a horn antenna.

Another important recent development is a technique called ‘phi-filtering’ [10] that can be used to extract any arbitrary 180- $\phi$  subset from a redundant SNF measurement [10].

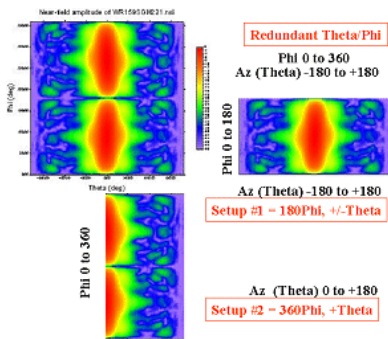


Figure 1. Diagram showing various SNF measurement geometries including redundant scan (top left), 360- $\phi$  (bottom left) and 180- $\phi$  (right)

Unlike the conventional 180- $\phi$  sphere, these extracted subsets can be centered at any  $\phi$ -position provided a 180° span is maintained. Figure 2. shows a sample redundant measurement where the phi-filter is centered at 0°, spanning  $-90^\circ \leq \phi \leq +90^\circ$ . The crucial benefit that this technique offers is that the “seams” of the sphere [7] can be located in regions of low energy and this reduces sensitivity to measurement drift and most importantly, misalignment.

### B. SNF Implementations

A number of SNF implementations are available. The most common type of system is the conventional phi-over-theta scanner ( $\phi/\theta$ ) shown in Figure 3. . The AUT is rotated about both  $\theta$  and  $\phi$  axes so that amplitude and phase data is acquired using a stationary probe. The  $\phi$ -axis is positioned horizontally, resulting in the AUT experiencing a changing gravity vector during acquisition. This is often undesirable or impossible for some devices.

Another common SNF implementation is the  $\theta/\phi$  variety. Here, the AUT is mounted on the positioner defining the  $\phi$ -axis and experiences the gravity vector in a fixed direction during acquisition. The near-field probe moves on a circular

trajectory around the AUT. This is especially useful for large, heavy antennas or any antenna that is gravitationally sensitive. This type of system facilitates AUT installation and reduces the effects of gravitational sag during measurement.

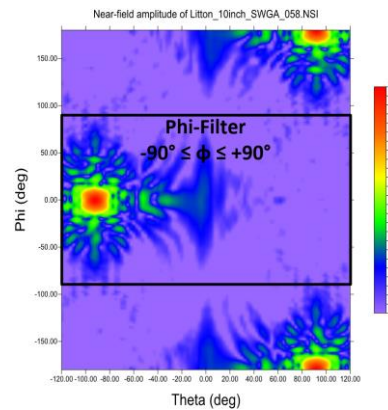


Figure 2. Phi-filter window slid to span the range  $-90^\circ < \phi < +90^\circ$

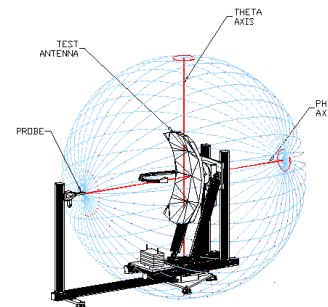


Figure 3. Illustration of a  $\phi/\theta$  SNF test system

NSI-MI recently installed a very large  $\theta/\phi$  SNF system for the US Navy in San Diego, CA. This system, shown in Figure 4. , was used to test a very heavy antenna that could not be easily turned on its side for practical reasons. This particular antenna radiates the majority of its energy toward the equator, near  $\theta = 90^\circ$ . The large size of this particular AUT and proximity of scattering bodies in the range necessitated the phi-filtering research reported on in [10].



Figure 4. US Navy  $\theta/\phi$  SNF system with very large AUT

#### IV. TEST CONFIGURATIONS

Several test scenarios were conducted in order to study the effect that spherical near-field alignment errors have on far-field results. Measurements were performed using an NSI-MI  $\theta/\phi$  test system with a 0.76 m probe arc radius and  $\pm 120^\circ$   $\theta$ -axis travel. The system's  $\theta = 0^\circ$  point was determined accurately using the laser alignment technique outlined in [1] prior to testing. Once this point was determined, it was used as a baseline for  $\theta$ -zero perturbation studies.

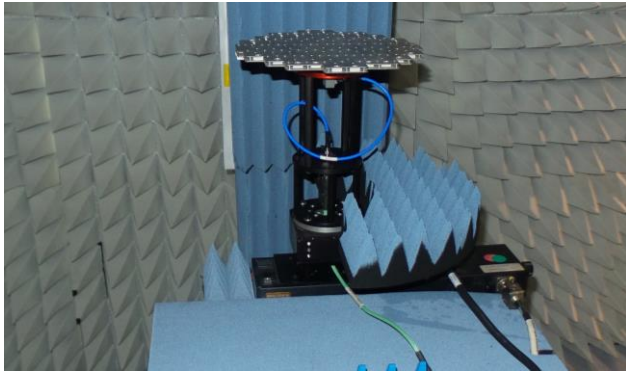


Figure 5. SWGA mounted in polar-mode with main beam radiating toward  $\theta = 0^\circ$ .

In addition to the three standard SNF rotation axes (theta, phi, polarization), this system was outfitted with a 10 cm linear translation stage used to move the  $\phi$ -stage rotator and AUT along the X-axis. Once properly aligned, this stage was used to induce known  $\theta/\phi$  non-intersection, accurate to within 25  $\mu\text{m}$ .

Two antennas were tested on this system, both at 9.375 GHz. First, a 25 cm x 25 cm slotted waveguide array (SWGA) was measured in two configurations:

1. Beam peak pointed toward the pole of the measurement sphere ( $\theta = 0^\circ$ , polar-mode). Figure 5. shows the SWGA mounted in polar-mode. Also shown is the 10 cm linear translation stage used for axis non-intersection adjustment.
2. Beam peak pointed toward the equator of the sphere ( $\theta = 90^\circ$ , equatorial-mode). Figure 6. shows the SWGA mounted in this orientation.

The peak directivity of this array was measured at 26.2 dBi in polar-mode and 26.0 dBi in equatorial-mode. The 0.2 dB difference is within the expected uncertainty for this configuration change.

The second antenna tested here was a broadband horn measured in polar-mode only. The lower directivity of the horn made it a poor candidate for measurements in equatorial mode where the effects of truncation in  $\theta$  would dominate all other sources of error.

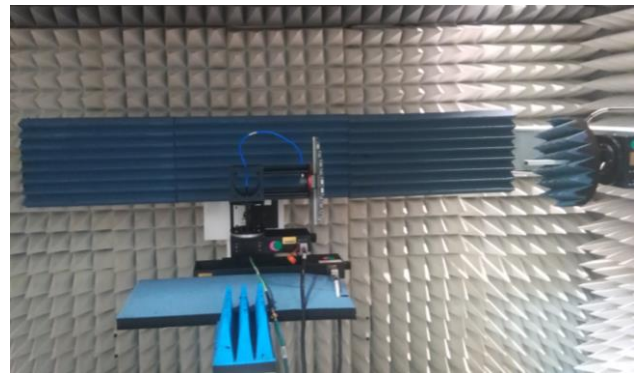


Figure 6. SWGA mounted in equatorial-mode shown with  $\theta = 90^\circ$

In addition to near-field measurements, a 5x5 dipole element array of  $0.5\lambda$  dipoles was simulated [11]. First, the array was contained within the X-Y plane to simulate a measurement where the peak of the pattern is pointed toward  $\theta = 0^\circ$  (polar-mode). Next, the same array was oriented within the Y-Z plane to simulate an equatorial measurement. Similar to the measured data,  $\theta/\phi$  non-intersection errors were introduced to study the effects and compare results. Table I. summarizes the five test cases to be analyzed in the next section.

TABLE I. MEASURED AND SIMULATED TEST SCENARIOS INVESTIGATED

AUT	Mounting Configuration	Peak Directivity (dBi)
10" SWGA	Polar	26.2
10" SWGA	Equatorial	26.0
Broadband Horn	Polar	18.7
Simulated 5x5 Array	Polar	18.8
Simulated 5x5 Array	Equatorial	18.4

#### V. ALIGNMENT SENSITIVITY RESULTS

##### A. Sensitivity to $\theta/\phi$ Non-Intersection Errors

Using the linear translation stage described, a maximum non-intersection (NI) error of 60.8 mm (1.9 $\lambda$  at 9.375 GHz) was achievable. Full SNF acquisitions were performed for a number of test cases spanning the  $0 \leq \text{NI-error} \leq 1.9\lambda$  range. The sub-sections below show sensitivities to some critical far-field parameters.

Peak directivity errors are plotted for all test cases as a function of NI error in this section. First, the redundant data sets acquired in polar-mode are shown in Figure 7. . The error for the simulated 5x5 array of dipoles agrees very well with the errors for the broadband horn, providing confidence that the measured data is not significantly affected by other sources of error outside of the scope of this work. The directivity of the higher gain SWGA is affected in a similar fashion but appears to be less sensitive to these errors overall.

Next, the same evaluation is done for a set of 180- $\phi$  test cases and results are shown in Figure 8. . In this set, the equatorial measurement of the SWGA and simulated array are included. It should be noted that the 180- $\phi$  subsets for the

polar-mode cases are extracted subsets of the redundant measurements shown in Figure 7. This is also true for the 360- $\phi$  subsets to be discussed next. The directivity errors resulting from the polar-mode measurements are smaller in magnitude than the redundant case. For the SWGA measured in equatorial-mode, the errors are less than 0.1 dB for the entire range of non-intersection errors and less than 0.3 dB for the entire range for the simulated array in equatorial-mode. It should be noted here that 180- $\phi$  measurements performed on an equatorially mounted antenna are very sensitive to the location of the near-field peak along the  $\phi$ -axis [9]. The measurement was configured such that the main beam was far from the edge of the 180°  $\phi$  span.

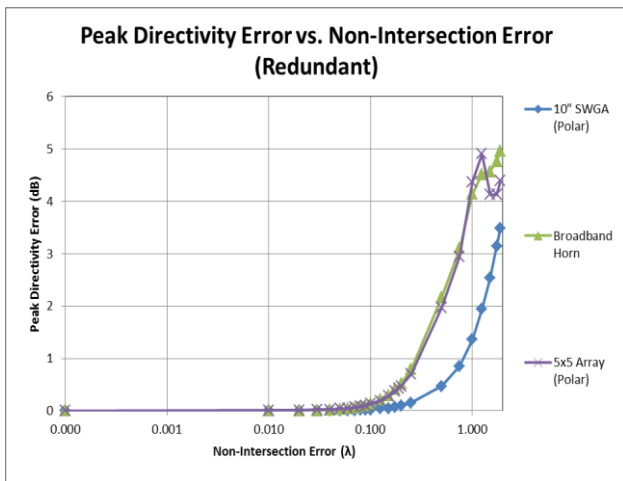


Figure 7. Peak directivity error vs. NI error for all test cases using redundant SNF data

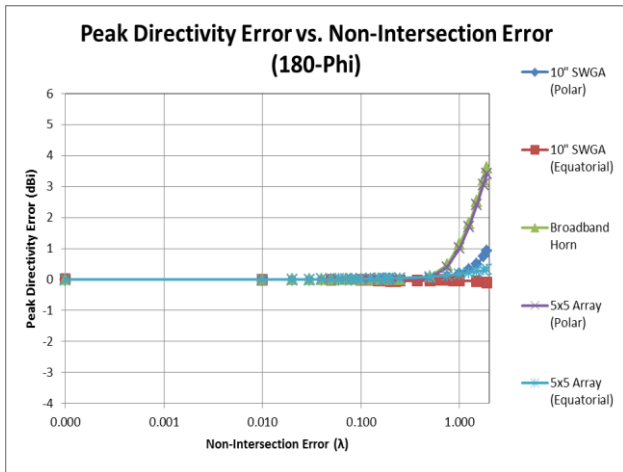


Figure 8. Peak directivity error vs. NI error for all test cases using 180- $\phi$  SNF data

Lastly, Figure 9. shows the impact of these NI errors on the 360- $\phi$  data sets. Once again, the directivity of the equatorial data sets shows virtually no sensitivity to this type of alignment error. The polar-mode datasets appear to be more sensitive than both the redundant and 180- $\phi$  cases, however.

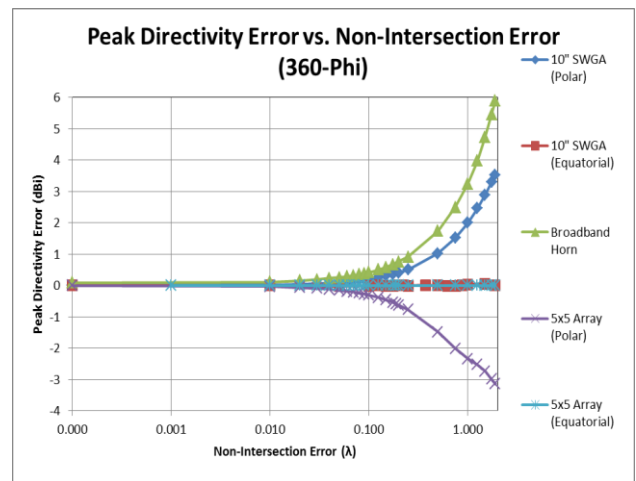


Figure 9. Peak directivity error vs. NI error for all test cases using 360- $\phi$  SNF data

In order to minimize the impact that a  $\theta/\phi$  NI error will have on peak directivity, an error threshold of  $\pm 0.1$  dB was chosen here. To meet this specification for all test cases, a non-intersection error better than  $0.09\lambda$  is required for the redundant geometry. For the 180- $\phi$  case, the NI error tolerance can be relaxed to as much as  $0.5\lambda$  to maintain the same  $\pm 0.1$  dB error threshold. Finally, for the 360- $\phi$  case, the non-intersection error must be controlled to less than  $0.05\lambda$  to maintain the same directivity error threshold. This can be especially challenging for high frequency applications. At 76 GHz, a common frequency for W-band automotive radar applications, the non-intersection error would need to be controlled to within 0.2 mm to support this error threshold for 360- $\phi$  polar-mode measurements. In this case, a 180- $\phi$  or redundant scheme would be preferred. The equatorial datasets analyzed here are insensitive to errors less than  $1\lambda$ .

### 1) Pattern Error Levels

NI errors will also affect the shape of a far-field pattern in ways that are not always evident in the directivity vs. frequency curve. To determine the sensitivity to these errors on the shape of the pattern, the perfectly aligned case (NI-error = 0) can be compared to all misaligned cases.

Figure 10. shows an example of this comparison on the principal plane azimuth cut for NI-error = 0 compared to NI-error =  $0.1\lambda$  for the SWGA in polar-mode. The resulting error-to-signal (E/S) level is calculated and plotted on the same curve. The resulting RMS and peak E/S levels (-57.4 dB and -50.1 dB, respectively) are recorded.

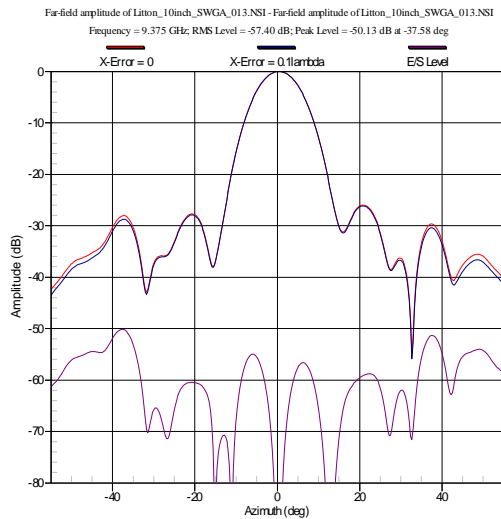


Figure 10. Azimuth cut comparison for the SWGA measured in polar-mode showing pattern difference between NI-error = 0 and  $0.1\lambda$ .

If these RMS and peak error levels are recorded for the range of non-intersection errors, the curves shown in Figure 11. and Figure 12. can be generated. Figure 11. shows these E/S levels for the SWGA measured in polar-mode for the redundant data set. Figure 12. shows the same curve for the broadband horn also measured in polar-mode. The resulting error levels for the broadband horn are higher across the range of NI errors.

Similar to the previous section, a threshold RMS pattern error level can be set to determine the maximum allowable NI error for a particular system. Here, an RMS E/S  $< -50$  dB is desired. In order to meet this specification for both antennas, the NI error should be less than  $0.1\lambda$ . It is likely that an even lower gain antenna than the horn would require a tighter tolerance to maintain the same  $-50$  dB threshold.

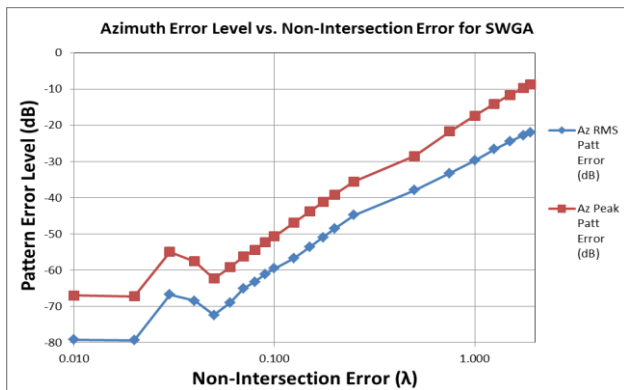


Figure 11. Azimuth cut peak and RMS pattern error level vs. NI error for the SWGA (polar-mode)

Figure 13. shows the results of this analysis for the SWGA processed using different grids (redundant,  $180\text{-}\phi$ ,  $360\text{-}\phi$ ). Unsurprisingly, the pattern error sensitivity to NI is different depending on the measurement grid selected. The results obtained by transforming the  $360\text{-}\phi$  subset are considerably worse than the redundant and  $180\text{-}\phi$  subsets, similar to the

directivity evaluation. A better alignment would be required to maintain the  $-50$  dB E/S threshold.

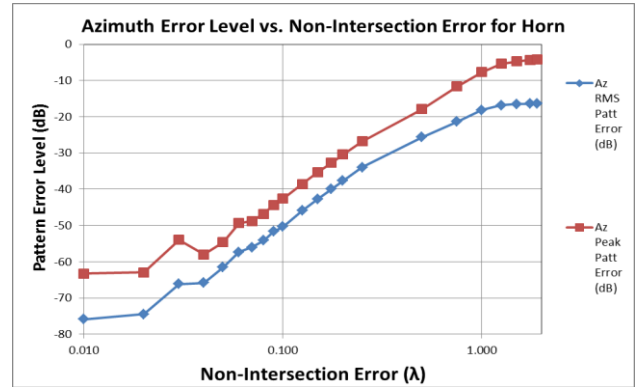


Figure 12. Azimuth cut peak and RMS pattern error level vs. NI error for the horn (polar-mode)

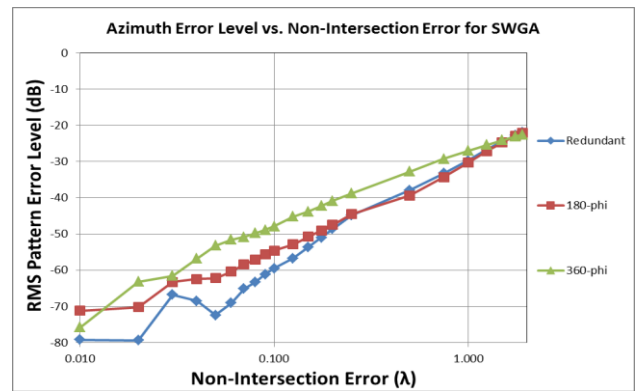


Figure 13. Azimuth cut RMS pattern error level for the SWGA showing redundant,  $180\text{-}\phi$  and  $360\text{-}\phi$  subsets

### B. Sensitivity to $\theta$ -Zero Errors

In order to determine the impact of  $\theta$ -zero errors on far-field results, the position defined as  $\theta = 0^\circ$  was modified from the well-aligned case to a maximum error of  $3.5^\circ$ .

Figure 14. shows the impact that  $\theta$ -zero errors have on the peak directivity for the SWGA. For both mounting configurations, a directivity error less than  $\pm 0.1$  dB is maintained provided the  $\theta$ -zero error is less than  $0.1^\circ$ . This is true for all measurement geometries (redundant,  $180\text{-}\phi$  &  $360\text{-}\phi$ ).

Polar measurements are sensitive to large  $\theta$ -zero errors and the chosen measurement grid will have an impact on the magnitude of these errors. For equatorial measurements, large  $\theta$ -zero errors appear to have little impact on the peak directivity when either grid is selected. When a  $180\text{-}\phi$  measurement is acquired, the span should be configured such that the main beam is far from the edge of the  $180^\circ \phi$  span. The  $180\text{-}\phi$  equatorial-mode results shown in Figure 14 are obtained from a phi-filtered measurement where the main beam was far from the edge of the  $180^\circ \phi$  span.

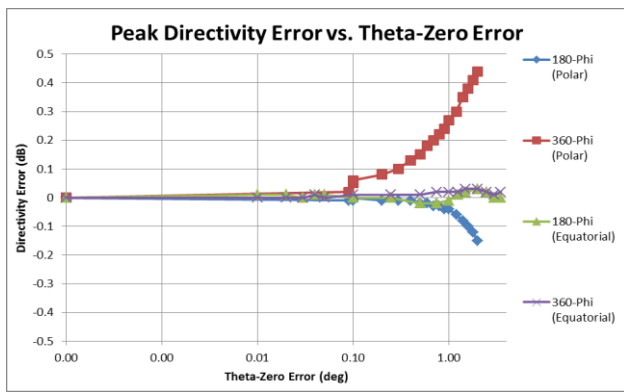


Figure 14. Peak directivity errors versus  $\theta$ -zero error for 180- $\phi$  and 360- $\phi$  SNF measurements

Figure 15. shows the near-field amplitude distribution for the SWGA using a phi-filter where the main beam is split between 0 and 180°, on the “seam” of the measurement sphere [7]. The resulting far-field pattern is then very sensitive to  $\theta$ -zero alignment errors. Very small phase errors between the phase of the two halves of the peak can lead to gross errors in the resulting far-field peak using this configuration.

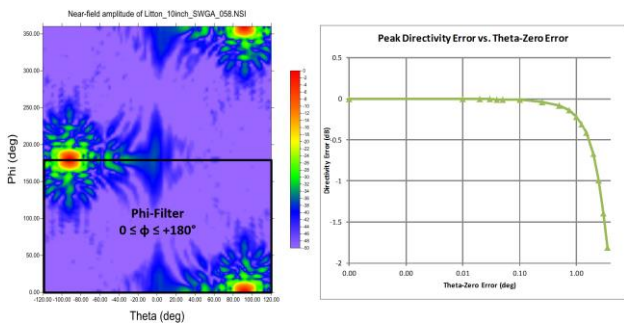


Figure 15. Phi-filter window showing main beam energy split at the edge of the measurement span (left) and resulting directivity error vs.  $\theta$ -zero error (right)

## VI. CONCLUSIONS

A number of tests were conducted on a  $\theta/\phi$  swing arm SNF scanner to quantify the sensitivity that axis NI and  $\theta$ -zero errors have on far-field radiation patterns. The peak directivity is nearly unaffected for equatorial measurements when either parameter is misaligned. For polar measurements, the chosen measurement grid will have an impact on the sensitivity to various errors. The peak directivity and pattern shape are less sensitive to errors for the 180- $\phi$  grid than the 360- $\phi$  alternative. In all cases, system alignment errors should be minimized in order to have confidence in the far-field pattern resulting from spherical near-field measurements. It is important for all 180- $\phi$  grid acquisitions to avoid locating the main beam on the edge or “seam” of the sphere since the slightest phase discontinuity in this region of high energy will adversely impact far-field derived results.

## VII. REFERENCES

- [1] J. Demas, “Low cost and high accuracy alignment methods for cylindrical and spherical near-field measurement systems”, in the proceedings of the 27th annual Meeting and Symposium, Newport, RI, USA, 2005.
- [2] S. W. Zieg, “A precision optical range alignment technique”, in the proceedings of the 4th annual AMTA meeting and symposium, 1982.
- [3] A.C. Newell and G. Hindman, “The alignment of a spherical near-field rotator using electrical measurements”, in the proceedings of the 19th annual AMTA meeting and symposium, Boston, MA, USA, 1997.
- [4] A.C. Newell and G. Hindman, “Quantifying the effect of position errors in spherical near-field measurements”, in the proceedings of the 20th annual AMTA meeting and symposium, Montreal, Canada, 1998.
- [5] A.C. Newell, G. Hindman and C. Stubenrauch, “The effect of measurement geometry on alignment errors in spherical near-field measurements”, in the proceedings of the 21st annual AMTA meeting and symposium, Monterey, CA, USA, 1999.
- [6] G. Hindman and A.C. Newell, “Spherical near-field self-comparison measurements”, in the proceedings of the 26th annual AMTA meeting and symposium, Atlanta, GA, USA, 2004.
- [7] C. Parini, S. Gregson, J. McCormick and D.J. van Rensburg, Theory and Practice of Modern Antenna Range Measurements. London, UK: The Institute of Engineering and Technology, 2015.
- [8] G. Hindman and A.C. Newell, “Mathematical absorber reflection suppression (MARS) for anechoic chamber evaluation and improvement”, in the proceedings of the 30th annual AMTA meeting and symposium, Boston, MA, USA, 2008.
- [9] A.C. Newell and G. Hindman, “Antenna pattern comparison using pattern subtraction and statistical analysis”, The 5th European Conference on Antennas and Propagation (EuCap), Rome, Italy, 2011.
- [10] G. Hindman, P. Pelland and G. Masters, “Spherical geometry selection used for error evaluation”, in the proceedings of the 37th annual AMTA meeting and symposium, Long Beach, CA, USA, 2015.
- [11] D. J. Janse van Rensburg, S R Mishra & Guy Séguin, “Simulation of errors in near-field facilities”, AMTA 17th Annual Meeting & Symposium, Williamsburg, Virginia, USA, Nov. 1995.

